Sheffield Hallam University

An iterative finite element method for piezoelectric energy harvesting composite with implementation to lifting structures under Gust Load Conditions

AKBAR, Mahesa and CURIEL-SOSA, JL

Available from Sheffield Hallam University Research Archive (SHURA) at:

https://shura.shu.ac.uk/34041/

This document is the Accepted Version [AM]

Citation:

Copyright and re-use policy

An Iterative Finite Element Method for Piezoelectric Energy Harvesting Composite with Implementation to An Aircraft Wingbox under Gust Load Conditions

M. Akbar*, J.L. Curiel-Sosa

Department of Mechanical Engineering, The University of Sheffield, Sir Frederick Mappin Building, Mappin Street, Sheffield, S1 3JD ,United Kingdom

Computer-Aided Aerospace and Mechanical Engineering Research Group (CA²M), The University of Sheffield, The Portobello Centre, Sheffield, S1 4ET, United Kingdom

Abstract

In this paper, a novel iterative finite element method (FEM) for energy harvesting purpose is presented. The new iterative FEM is implemented to solve the dynamic problems of piezoelectric-based energy harvester in the frequency and time domains. The validation against other methods from the literature shows the robustness and capabilities of the iterative FEM. Implementation to a transport aircraft wingbox with 14.5 m half span and an embedded piezoelectric layer is shown in some details. The energy harvesting potential of the wingbox due to the cruise and the 1-cosine gust loads is investigated. In addition, for the first time, stress and failure analyses of the structure with an active energy harvesting layer are performed. The results pointed out that the wingbox is still in a safe condition even when it is subjected to a 30 m/s gust amplitude while harvesting 51 kW power.

Keywords: Piezoelectric, Energy Harvesting, Iterative FEM, 1-Cosine Gust, Aircraft Wingbox

1. Introduction

The renewable energy potential from ambient sources, i.e., solar, wind, thermal, lead to the development of innovative power generator systems from micro to macro scale [1–3]. In the past decade, studies on the multifunctional material system have shown a promising feature in combining energy generation with the structural function, i.e., load-bearing [4]. Implementation of this technology in the aerospace field has also been discussed in the literature [5].

In the present work, a study on the multifunctional material system focusing on the piezoelectric energy harvesting potential from aircraft structure is performed. Anton and Inman [6] performed one of the earliest tests on the piezoelectric energy harvesting from a small aircraft structure. Investigations on lifting structure and flow-induced vibration energy harvesting have been in extensive development since [7].

Analytical and numerical models have become favourable tools to evaluate piezoelectric energy harvesting from flow-induced vibration [8]. Erturk et al. introduced the piezoaeroelastic term and provided an experimentally validated analytical model for a flutter-based energy harvesting from 2-DoF airfoil in [9]. An increase in the flutter instability limit due to the piezoelectric shunt damping was found from their investigation. Extension of this work can be seen in the electromagnetic airfoil [10], the hybrid piezo-electromagnetic [11] and the 3-DOF airfoil with control surface [12] models.

Moreover, the airfoil flutter model of Erturk et al. [9] is further developed to a lifting surface model in [13–15]. A preliminary model of the piezoaeroelastic planar lifting surface is given in [13]. This model utilises the combination of an electromechanically coupled FEM and a time-domain unsteady aerodynamic model via the Vortex-Lattice Method (VLM). The model was further elaborated in [14] to evaluate the energy harvesting potential of a plate-like wing under excitation of different airspeed condition, and the effect of aerodynamic damping to the system was

discussed. The frequency-domain unsteady aerodynamic model, Doublet-Lattice Method (DLM), was used in [15] to perform the flutter analysis of the plate-like wing. In agreement with [9], they found that the shunt damping effect increased the critical flutter speed.

The structural model in [13–15] utilised the laminated quadrilateral shell element developed by De Marqui et al. in [16]. Apart from the 3-DOF displacement, one vertical translation and two rotations, on each node, a voltage degree of freedom is added to each element. To the authors' knowledge, to this date, this work is one of the few that successfully modelled a plate-like energy harvester with three-dimensional motion via an electromechanically coupled finite element model. This model further advanced for the analysis of energy harvesting from a functionally graded piezoelectric composite plate in [17, 18].

In contrast with the finite element model of [16] which require numerical code development, some efforts have been made to utilise commercial FEM and computational fluid dynamic (CFD) software for the energy harvesting simulation such as presented in [19–23]. Those models have been experimentally well validated, however, the analyses were only performed for short-circuit (no resistance load, $R \to 0$) or open-circuit ($R \to \infty$) problems. Thus, there was no variation to the resistance load.

An attempt of using 3D finite elements of commercial software to evaluate the effect of the resistance load variation is given in [24]. However, validation by other methods was not conducted in the investigation. Furthermore, the governing equation applied to their finite element model depicted the whole effect of the electromechanical coupling and capacitance as the analogues of the stiffness. This approach is in contrast with the model in [16], in which the capacitance and a part of electromechanical coupling are the analogues of damping and associated with the velocity.

Other efforts performed numerical investigation via the analogue of the piezoelectric energy harvester structure with the electrical circuit model. In [25], parameter identification on a finite element model was conducted to construct an equivalent circuit model which was simulated in an integrated circuit simulator software. In opposite, the investigation in [26] constructed the equivalent of the structural model from the electrical parameters which was input to a

commercial finite element software. Meanwhile, the investigation presented in [27] attempted to couple a finite element model with a circuit modeller software.

In recent studies, [28, 29], advanced beam elements comprising 3D effects have been developed to model the piezoelectric energy harvester. The use of beam element for fluid-structure interaction is presented [30]. Iterative scheme between beam elements and aerodynamic loads modelled via the Reynolds-averaged Navier-stokes (RANS) was developed. Simulation of energy harvester plate exerted by the wake of on a cylinder was performed.

Detailed reviews on numerous studies of the piezoaeroelastic energy harvesting are given [7, 8, 31–33]. Although significant attention was given to the piezoaeroelastic energy harvesting, the lack of study on a more practical aerodynamic loading is concerned [8]. As reviewed in [31], Mainly the studies focused on resonance and instability phenomenon, i.e., Vortex-Induced Vibration, flutter. To the authors' knowledge, in addition to the works done by De marqui et al. [13, 14], only a few articles [34–39] presented the evaluation of the lifting structure under a more practical aerodynamic loading condition, i.e., cruise and gust loads.

Xiang et al. [34] and Bruni et al. [35] investigated discrete gust loading conditions, i.e., 1-cosine and square gusts. Xiang et al. [34] modelled a UAV wingbox structure using beam elements with discrete masses and stiffnesses obtained from a step function. Whereas Bruni et al. [35] utilised lumped parameters to model the masses and stiffnesses of a slender wing. Both investigations applied the aerodynamic loading via the Strip theory. Meanwhile, Tsushima and Su in [36] developed a model to evaluate random gust/ turbulence condition. Beam elements were also used to discretise the structure and coupled with a 2D airfoil unsteady aerodynamic model. In [37], This model was extended to include active control function.

Harmonic cruise loading condition was investigated by Akbar and Curiel-Sosa in [38]. A hybrid analytical/FEM scheme was proposed. The structural dynamic responses obtained from commercial FEM software were coupled with the governing voltage equations of the piezoelectric composite to obtain the energy harvesting solution. This hybrid scheme was implemented to evaluate energy harvesting potential from a wingbox of a civil jet transport aircraft. Further discussed in [40], a faster computational time was benefitted from this hybrid scheme compared to the
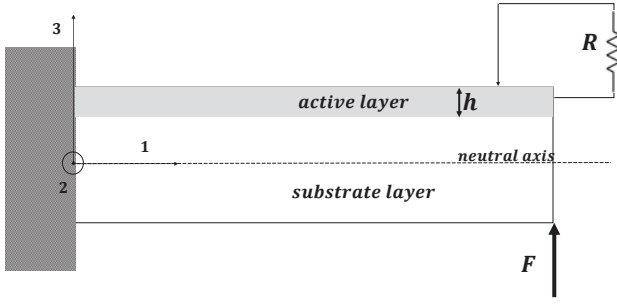
2

Figure 1: A cantilevered piezoelectric composite energy harvester exerted by a mechanical force, F, and an electrical resistance load, R

full electromechanically coupled FEM of [16]. The hybrid scheme was further elaborated in [39]. Multiphase piezoelectric composites were implemented to the aircraft wingbox to obtain better weight - energy optimisation. The results pointed out up to 40 kW of power can be generated and reduced the fuel consumption.

Despite the fact that the models built in [13, 14, 34–37] provided the platforms to evaluate the energy harvesting potential from the lifting structure under cruise/gust loads, to the authors' knowledge, comparison with other methods have not yet been conducted. Only the hybrid scheme in [38, 40] has been validated with analytical and FEM solutions, although the approach was only compared to the base excitation problem of [41]. Therefore, in the present work, a novel computational method to evaluate the energy harvesting on the lifting structure is developed.

An innovative iterative FEM for energy harvesting purpose is proposed here. This method is able to perform energy harvesting solution utilising FEM and aerodynamic modules from the commercial software with minimum support of a computational code. Hence, provides capabilities in evaluating various loading cases and complicated structure with the flexibility to use a different type of finite elements, i.e, solid, shell, laminated shell for composite. The comparisons against the gust loading models of [14, 34], as well as the classical benchmark of the base excitation model [41] are presented in this paper. The investigation to verify the energy harvesting potential of the aircraft wingbox of [39] is also shown in some details. The mathematical model and computational algorithm of the iterative FEM are explained in the following sections.

2. Iterative FEM

In the governing equations of the piezoelectric energy harvester used in the present work, the stress-charge form is adopted. Based on the IEEE standard [42], the stress-charge form is expressed as

$$
\boldsymbol{\Sigma} = \begin{bmatrix} \mathbf{C} & -\mathbf{e}^T \\ (6 \times 6) & (6 \times 3) \\ \mathbf{e} & \varepsilon^{\boldsymbol{S}} \\ (3 \times 6) & (3 \times 3) \end{bmatrix} \tag{1}
$$

The transformation from the stress-charge form to strain-charge form can be written as

$$
\begin{aligned}
\mathbf{C} &= \mathbf{S}^{-1} \\
\mathbf{e} &= \mathbf{d}\, \mathbf{S}^{-1} \\
\varepsilon^{\boldsymbol{S}} &= \varepsilon^{\boldsymbol{T}} - \mathbf{d}\, \mathbf{S}^{-1}\, \mathbf{d}^t
\end{aligned} \tag{2}
$$

where the symmetries due to orthotropic, i.e., $C_{11} = C_{22}$, $d_{31} = d_{32}$, etc., are directly applied. $\mathbf{C}$ and $\mathbf{S}$ are the stiffness/elasticity matrix and the compliance matrix, respectively. The piezoelectric coupling constants in stress-charge and strain-charge forms are defined by $\mathbf{e}$ and $\mathbf{d}$. The piezoelectric constant, $\mathbf{d}$ also called as the charge constant. The permittivity in stress-charge and strain-charge forms are represented by $\varepsilon^{\boldsymbol{S}}$ and $\varepsilon^{\boldsymbol{T}}$. The permittivity of the material often written as relative permittivity, non-dimensionalised by the vacuum permittivity, $\varepsilon_0 = 8.85 \times 10^{-12}$ F/m.

A typical geometry of the a cantilevered piezoelectric composite energy harvester is shown in Figure 1. The active layer is the piezoelectric layer and the substrate layer made of non-piezoelectric material. The following convention is followed, the 3-direction refer to the polling in the thickness direction and the 1-direction is in the longitudinal (spanwise) direction.

2.1. The Coupled Electro-mechanical Equations

In the present work, the piezoelectric electromechanical equilibrium in a dynamic problem is concerned. The governing equation of a coupled mechanical - electrical actuation problem for piezoelectric finite elements [43] is modified to obtain the energy harvesting solution. This actuation problem can be written as follows

$$
\begin{bmatrix} \mathbf{M} & \mathbf{0} \\ \mathbf{0} & \mathbf{0} \end{bmatrix} \left\{ \begin{matrix} \ddot{\mathbf{U}} \\ \ddot{\mathbf{V}} \end{matrix} \right\} + \begin{bmatrix} \mathbf{G} & \mathbf{0} \\ -\mathbf{K_{vu}} & \mathbf{K_{vv}} \end{bmatrix} \left\{ \begin{matrix} \dot{\mathbf{U}} \\ \dot{\mathbf{V}} \end{matrix} \right\} + \\
\begin{bmatrix} \mathbf{K_{uu}} & \mathbf{K_{uv}} \\ \mathbf{0} & \mathbf{0} \end{bmatrix} \left\{ \begin{matrix} \mathbf{U} \\ \mathbf{V} \end{matrix} \right\} = \left\{ \begin{matrix} \mathbf{F} \\ \dot{\mathbf{Q}} \end{matrix} \right\} \tag{3}
$$

3

The sizes of the matrices in Equation (3) are defined by the number of degrees of freedom in mechanical, n_m, and electrical, n_e, domains [16]. The first and second derivatives with respect to the time are denoted by the dot, $[\dot{\ }]$, and the double dots, $[\ddot{\ }]$. Here, $\mathbf{U}$ $(n_m \times 1)$, $\mathbf{V}$ $(n_e \times 1)$, $\mathbf{F}$ $(n_m \times 1)$ and $\dot{\mathbf{Q}}$ $(n_e \times 1)$, respectively, are the global nodal displacement, electrical voltage, mechanical force and electrical current vectors of the element. $\mathbf{M}$ $(n_m \times n_m)$ and $\mathbf{G}$ $(n_m \times n_m)$ represent the global mass and mechanical damping matrices. The global stiffness and dampring matrices concerning the electromechanical system are denoted by $\mathbf{K_{uu}}$ $(n_m \times n_m)$, $\mathbf{K_{uv}}$ $(n_m \times n_e)$, $\mathbf{K_{vu}}$ $(n_e \times n_m)$ and $\mathbf{K_{vv}}$ $(n_e \times n_e)$. These global matrices are assembled from the associated element's matrices as follows [44]

$$\mathbf{K_{uu}^e} = \int_{Vol} \mathbf{B}^T \, \mathbf{C} \, \mathbf{B} \, dVol \qquad (4)$$

$$\mathbf{K_{vv}^e} = \int_{Vol} \mathbf{B_E}^T \, \varepsilon^S \, \mathbf{B_E} \, dVol \qquad (5)$$

$$\mathbf{K_{uv}^e} = \int_{Vol} \mathbf{B}^T \, \mathbf{e}^T \, \mathbf{B_E} \, dVol \qquad (6)$$

$$\mathbf{K_{vu}^e} = \int_{Vol} \mathbf{B_E}^T \, \mathbf{e} \, \mathbf{B} \, dVol \qquad (7)$$

$$\mathbf{M^e} = \int_{Vol} \mathbf{N}^T \, \rho \, \mathbf{N} \, dVol \qquad (8)$$

Equations (4-8) represent the element's volume integral of the associated constitutive components in Equation (1). The density of the material is defined as ρ. The superscript $\mathbf{e}$ denotes the matrix of an element. The structural stiffness matrix, $\mathbf{K_{uu}^e}$, is constructed from the elasticity matrix. Whereas $\mathbf{K_{vv}^e}$ is the capacitance of the piezoelectric element. The electromechanical coupling of the piezoelectric element is represented by $\mathbf{K_{uv}^e}$ and $\mathbf{K_{vu}^e}$ matrices. $\mathbf{B}$ and $\mathbf{B_E}$ involves the shape functions, $\mathbf{N}$, of the element based on the type of discretisation [45]. In the present work, the poling of the piezoelectric layer is assumed in the thickness direction. Hence, the component inside the integral of Equation (5) can be expressed as [16]

$$\mathbf{B_E}^T \varepsilon^S \mathbf{B_E} = \frac{\varepsilon^S_{33}}{h^2} \qquad (9)$$

In addition, the piezoelectric materials usually manufactured as a thin plate and sandwiched between very thin and conductive electrodes. Therefore, if the continuous electrodes are used on the whole surfaces, all elements can be assumed to generate the same voltage. Thus, vector $\mathbf{V}$ reduces to a voltage V [16]. Hence,

$$\mathbf{K_{uv}} \mathbf{V} = \mathbf{K_{uv}}[1\ 1...1]^T V = \mathbf{K_{uv}^*} V \qquad (10)$$

where the size of the ones vector $[1\ 1...1]^T$ is $n_e \times 1$, and the electromechanical coupling is now defined by the vector $\mathbf{K_{uv}^*}$ $(n_m \times 1)$.

To modify the actuation problem in Equation (3), the current, $\mathbf{I} = \dot{\mathbf{Q}}$, is defined not as an input, but, as the function of the voltage output from the piezoelectric harvester. The electrical load, however, came from an external circuit connected to the structure as shown in Figure 1. In the present work, the resistance load, R, is applied as the the electrical load, thus, $\dot{\mathbf{Q}} = -\frac{V}{R}$. Therefore, Equation (3) can be written as

$$\mathbf{M\ddot{U}} + \mathbf{G\dot{U}} + \mathbf{K_{uu}U} = \mathbf{F} - \mathbf{K_{uv}^*}V \qquad (11)$$

, and

$$-\mathbf{K_{vu}^*}\dot{\mathbf{U}} + K_{vv}\dot{V} + \frac{V}{R} = 0 \qquad (12)$$

where vector $\mathbf{K_{vu}^*} = \mathbf{K_{uv}^*}^T$ and K_{vv} is the capacitance of the piezoelectric layer.

The idea of the present iterative FEM is to obtain the solution of the displacement vector $\mathbf{U}$ of the structure and the voltage output, V, of the piezoelectric layer through an iterative process between Equations (11) and (12). This iteration process allows Equation (11) to be separately solved as if it is an "actuation" problem with the mechanical force, $\mathbf{F}$, and the voltage, V, as the actuating load to deform the structure. In the iteration process, Equation (12) will update the value of the voltage V on each iteration based on the displacement vector solved by Equation (11). A more detailed algorithm of the present iterative FEM is described in Section 2.2. In addition, the harvested power, P, is expressed as

$$P = \frac{V^2}{R} \qquad (13)$$

For an undamped harmonic oscillation motion, the displacement, voltage and force are assumed as the function of an excitation frequency, ω (rad/s) and can be written as

$$\mathbf{U} = \mathbf{\bar{U}}e^{i\omega t}$$
$$\mathbf{F} = \mathbf{\bar{F}}e^{i\omega t} \qquad (14)$$
$$V = \bar{V}e^{i\omega t}$$

4

where $i = \sqrt{-1}$ and the bar above a parameter denotes the amplitude. Hence, Equations (11) and (12) become

$$-\omega^2 \mathbf{M}\bar{\mathbf{U}} + \mathbf{K_{uu}}\bar{\mathbf{U}} = \bar{\mathbf{F}} - \mathbf{K_{uv}^*}\bar{V} \qquad (15)$$

, and

$$\bar{V} = \frac{i\omega\mathbf{K_{vu}^*}\bar{\mathbf{U}}}{i\omega K_{vv} + \frac{1}{R}} \qquad (16)$$

Therefore, in this case, the iteration process will involve Equations (15) and (16).

2.2. Computational Scheme

In the present iterative FEM, one of the unique features is the seclusion of Equation (11) to be solved as if it is an actuator problem. The actuator problem is already a matured problem in the structural analysis field, and the module is readily available in many commercial finite element software, i.e., Abaqus, Ansys, MSC Nastran [46]. Therefore, the present iterative FEM provides excellent ease for utilising the standard commercial software. In addition, Equation (12) can be solved with minimum computational coding.

Moreover, the ease of solving Equation 11 via an already established computational software is that the mechanical force, $\mathbf{F}$, may have a wide range of form, i.e., concentrated force, pressure, relative motion, or combination of several load types. Sections 3-6 present the works which demonstrate the implementation of base excitation motion and unsteady aerodynamic loads as the mechanical force. Moreover, the mechanical damping, $\mathbf{G}$, can also be modelled with various form [47], i.e., proportional to the stiffness matrix (structural damping), the linear combination of mass and stiffness matrix (Rayleigh damping), the function of natural frequency (modal damping).

Prior to entering the iteration process, one essential parameter to be obtained is the electromechanical coupling vector, K_{uv}^*. This vector can be extracted from the commercial software by solving first a dummy static actuator simulation with a unit voltage load, i.e., 1V, and no mechanical load. In the case of static analysis, Equation (11) reduces into

$$\mathbf{K_{uu}}\mathbf{U} = -\mathbf{K_{uv}^*}V \qquad (17)$$

Hence, the commercial software will calculate a forcing vector on the nodes only as a function of $\mathbf{K_{uv}^*}$. This forcing vector can usually be found in the input file created by the software. To be noted, however,

the negative sign on the right-hand side (RHS) of Equation (17) represents the internal force generated by the reverse piezoelectric effect. Hence, as the commercial software treats the RHS as an external actuating force, the negative sign needs to be added to the extracted forcing vector or the input voltage of the commercial software. This rule also applies when applying the voltage to the commercial software during the iteration process.

In some software, electrical actuator solution is evaluated via the thermal actuator analogy [46]. The thermal expansion coefficient vector, α, is used to represent the piezoelectric charge constants, $\mathbf{d}$. Concerning the thermal forcing function, the analogy can be seen as follows [43]

$$\mathbf{RHS_{thermal}} = \int_{Vol} \mathbf{B}^T \, \mathbf{C} \, \boldsymbol{\alpha}^T \, T \, dVol \qquad (18)$$

$$\mathbf{K_{uv}^*}V = \int_{Vol} \mathbf{B}^T \, \mathbf{C} \, \tilde{\mathbf{d}}^T \, E \, dVol \qquad (19)$$

where the electrical field is $E = V/h$ and the piezoelectric charge constants matrix $\mathbf{d}$ (3×6) is collapsed to the vector $\tilde{\mathbf{d}}$ (1×6). This vector is expressed as

$$\tilde{\mathbf{d}}^T = [d_{31} \; d_{32} \; d_{33} \; 0 \; 0 \; 0]^T \qquad (20)$$

which analogous to the thermal expansion coefficient vector as

$$\boldsymbol{\alpha}^T = [\alpha_1 \; \alpha_2 \; \alpha_3 \; \alpha_4 \; \alpha_5 \; \alpha_6]^T \qquad (21)$$

Hence, in the case thermal actuator module is used, the piezoelectric charge constants per layer thickness are input as the thermal expansion coefficients, i.e., $d_{31}/h = \alpha_1$, and the voltage as the temperature, i.e., $V = T$, to the commercial software.

The algorithm of the time-domain iterative FEM is depicted in Figure 2a. In the present work, the computational code to solve Equation (12) is built using MATLAB$^{\copyright}$. The ordinary differential equation (ODE) solver of MATLAB$^{\copyright}$ is used to obtain the solution of $V(t)$ for each iteration.

Initially, Equation (11) is solved in the commercial software by assuming no voltage applied, $V^0 = 0$. The initial value of velocity vector, $\dot{\mathbf{U}}^0$, is then used as input to the computational code to obtain the first solution of the harvested voltage, $V(t)^1$, via Equation 12. This first solution, $V(t)^1$, is input to Equation (11) to obtain the new velocity vector of iteration.
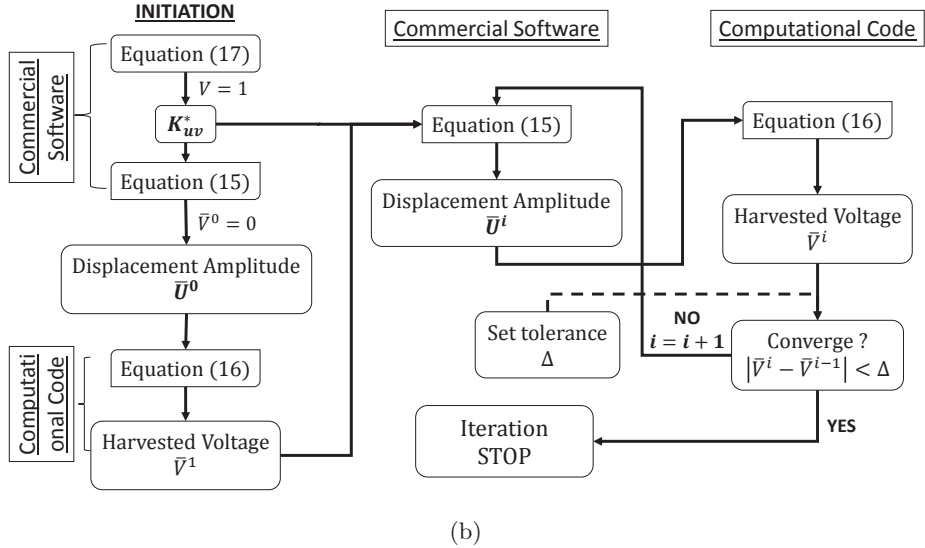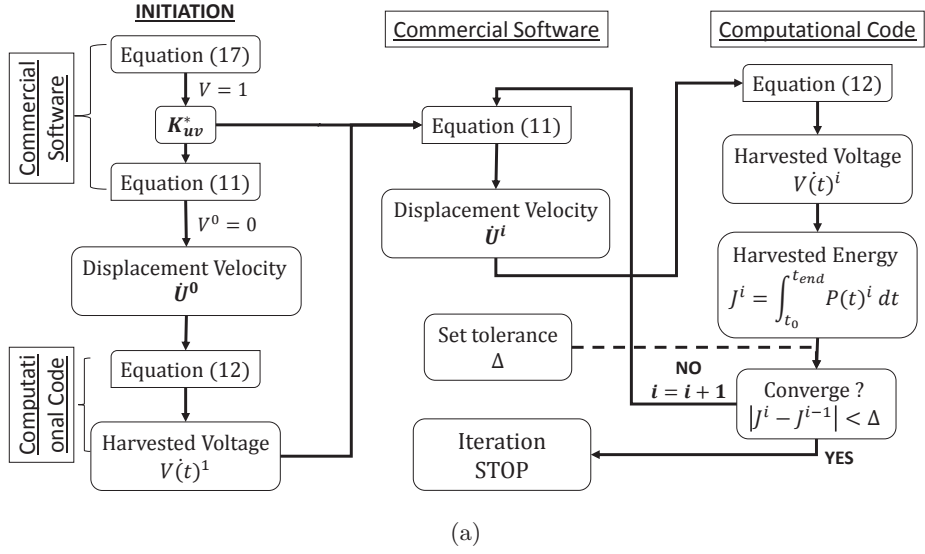
5

Figure 2: The workflow of the iterative FEM for (a) time domain and (b) frequency domain problems

This new velocity vector then inputs again to solve Equation (12). This process is repeated until the solution is converged.

In the present work, the convergence criteria for the time domain simulation is based on the variance of energy from the current iteration and the previous iteration, $J^i - J^{i-1} < \Delta$. In addition, the voltage function, $V(t)$, the trend is also observed to ensure that the patterns are similar and in reasonable shape on each iteration.

The iteration process for the frequency domain is shown in Figure 2b. In this case, Equations (15) and (16) are the main governing equations. In addition, the iterative variables for the frequency domain case are the amplitudes, $\mathbf{U}$ and V. Hence, the convergence

criteria also much simpler by comparing the variance of the voltage from each iteration, $V^i - V^{i-1} < \Delta$.

3. Unimorph Plate under Base Excitation

In this section, the energy harvesting evaluation of a unimorph exerted by base excitation is presented in [41]. The iterative FEM for frequency and time domain is utilised. Comparison against the result of Erturk-Inman's analytical model [41] is also shown in some details.

The unimorph plate consisted of a host structure (isotropic metal) and a piezoelectric layer (PZT-5A) covering the top surface of the plate similar to the configuration shown in Figure 1. The size of the plate

6

is $100 \times 20 \times 0.9$ mm^3 (length $\times$ width $\times$ thickness), with PZT covering 44% of the thickness. The details of the material properties for a beam-type formulation can be found in [41]. However, as solid and shell elements are used here, the 3D and 2D material properties of PZT-5A in [48] are utilised.

The verification of the unimorph structural models is performed by means of modal analysis. The unimorph is modeled by 25×5 elements, in the spanwise and the chordwise directions, respectively. For solid model, each layer on thickness direction is made of their own respective material (PZT or metal). However, for shell model, the laminated composite module is used to represent the lay-up sequence.

The natural frequencies and the mode shapes of the present structural models are depicted in Table 1. The results of Erturk-Inman's analytical model is displayed in column "Anly.", while the present models' are shown in columns "Present-Solid" and "Present-Shell". The first, second and third bending modes are denoted by "1B", "2B" and "3B", respectively. It can be seen that both solid and shell models natural frequencies are in a good agreement against analytical results in [41] with insignificant variances, $\Delta \leq 1\%$.

Table 1: Natural frequency comparison of the unimorph

| Mode Shape | Natural Frequency (Hz) | | | | |
	Anly. [41]	Present - Solid	Δ	Present - Shell	Δ
1B	47.8	47.8	0.00%	47.5	0.63%
2B	299.6	299.3	0.10%	296.9	1.00%
3B	838.2	841.1	0.35%	831.9	0.75%

In the frequency domain investigation, $1\mu m$ amplitude of vertical displacement is applied at the root as the base excitation load. The excitation frequency is equal with the first bending natural frequency. Resistance load of 15 kΩ is used as the external electrical load. As previously explained in Section 2, initially a pure structural dynamic response without voltage load is performed to start the iteration process. Following the iterative procedure in Section 2, on each iteration step, the voltage output and the structural responses are updated.

The voltage and relative tip amplitudes on each iteration step for both solid and shell models are depicted in Figures 3 and 4. The dotted line with green circles denote the results of the iterative FEM on each iteration step. The references' values denoted by straight red line and black dashed line are ob-

tained via Erturk-Inman model [41] and Akbar & Curiel-Sosa hybrid analytical/computational scheme [38]. However, with the hybrid scheme, only the voltage amplitude can be compared as the structural displacement after affected by voltage response is not viable from this approach.
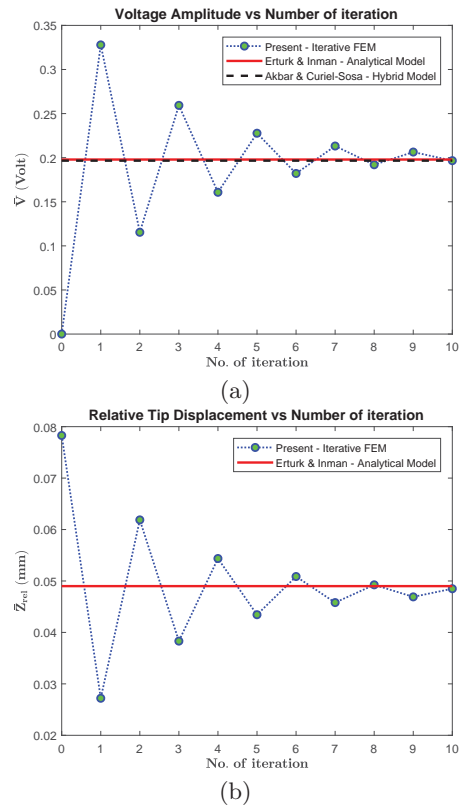

Figure 3: The iteration histories of (a) voltage and (b) relative tip displacement amplitudes of the unimorph modeled by solid elements

It can be seen in Figures 3a and 4a, initial value of voltage amplitude, $\bar{V}$, is zero. This condition resulted in a pure mechanical structural response with relative tip displacement, $\bar{Z}_{rel}$, around 0.08 mm as depicted in Figures 3b and 4b. The first iteration updated these values with the existence of voltage output and a much lower tip displacement around 0.03 mm. The iteration histories shown in Figures 3 and 4 display the fluctuation on both voltage and tip displacement amplitudes around the references' values until they converge to some particular points.

The fluctuation happens as the electromechanical coupling tries to balance the responses exerted by the mechanical load and the reverse piezoelectric effect. Initially, a small voltage at an iteration step, i, resulted in a large displacement caused mainly by the mechanical load, $Z^i_{mech} >>> Z^i_{elec}$, hence,
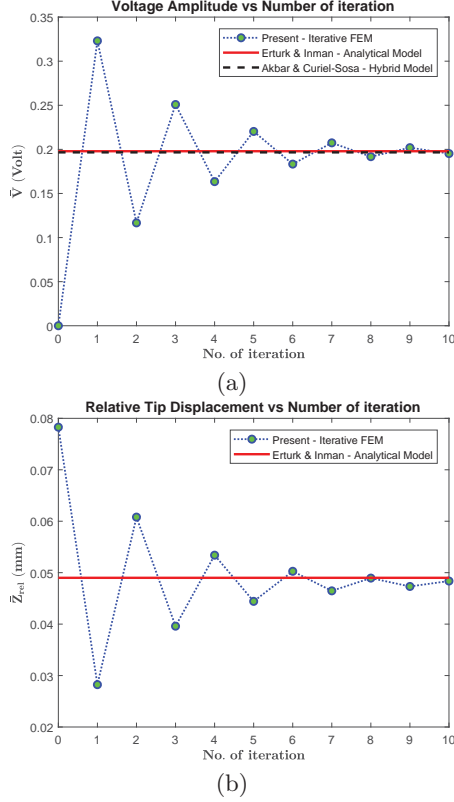
7

(a)

(b)

Figure 4: The iteration histories of (a) voltage and (b) relative tip displacement amplitudes of the unimorph modeled by shell elements

$Z_{total}^i \approx Z_{mech}^i$. However, large displacement means a larger voltage as the input for the next iteration, $i+1$. Hence, the displacement due to electrical load will be larger, $Z_{elec}^{i+1} > Z_{elec}^i$. Due to reverse piezoelectric effect as explained in Section 2, as Z_{elec} is in the opposite direction of Z_{mech}, thus, the total displacement is reduced, $Z_{total}^{i+1} < Z_{total}^i$. On the next iteration, however, this means smaller voltage, hence, $Z_{elec}^{i+2} < Z_{elec}^{i+1}$, and $Z_{total}^{i+2} < Z_{total}^{i+1}$. The iteration process will goes on in this cycle until the total displacement is consisted of proper amounts of Z_{elec} and Z_{mech}.

In more details, the iteration histories are shown in Tables 2 and 3. Initially, the iteration variances are more than 60% for both voltage and displacement amplitudes. However, only with 10 iteration steps, the iteration variances significantly reduce to less than 5%. Table 4 depicted in detail the comparison of the present iterative fem results with the references' values. The present results for both solid and shell models are in close comparison to the references' with variances only around 1%.

For iterative FEM simulation in time domain, the input of vertical displacement at the root is given

Table 2: Voltage amplitude for each iteration of the unimorph modeled by solid elements

Iteration	$\bar{V}$ (Volt)	Variance
1	0.3279	
2	0.1154	$\Delta_{1-2} = 64.80\%$
9	0.2064	
10	0.1966	$\Delta_{9-10} = 4.75\%$

Table 3: Tip displacement amplitude for each iteration of the unimorph modeled by solid elements

Iteration	$\bar{Z}_{rel}$ (mm)	Variance
0	0.0783	
1	0.0272	$\Delta_{0-1} = 65.26\%$
9	0.0469	
10	0.0485	$\Delta_{9-10} = 3.30\%$

at each time step following the harmonic oscillation motion, $Z(0,t) = \bar{Z}(0)e^{i\omega t}$. In the present case, a tabular input of the root displacement with 0.1 ms time step is applied. As explained in Section 2, in the time domain scheme, the voltage and velocity responses for each time step are updated on each time step. As expected, the final iteration results of the time domain scheme closely follows the trend of the frequency domain's as shown in Figure 5. The iterative FEM in time domain is further elaborated in the following sections.

4. Bimorph plate under Gust Load Conditions

The energy harvesting evaluation of piezoelectric embedded lifting surfaces/structures exposed to a freestream flow and gust wind are presented in this section as well as Sections 5 and 6. Herein, only a brief introduction of gust loading condition is described. Interested reader on gust and aeroelasticity loads is referred to a more detailed discussion in [49]. Figure 6 displays a general illustration of a discrete gust wind in the form of 1-cosine gust with a gust length, L_g.

In Figure 6, the lifting surface flies with a speed, V_∞ entering the gust wind regime. The distance and time of the gust penetrating the lifting surface are denoted by S_g and t_g, respectively. The gust gradient distance, H_g, is the distance to reach the maximum gust speed, V_{g_0}, in which $L_g = 2H_g$. The variation of the gust speed, V_g, to the time t_g is defined as

8

Table 4: Voltage and relative tip displacment amplitudes comparison of the unimorph

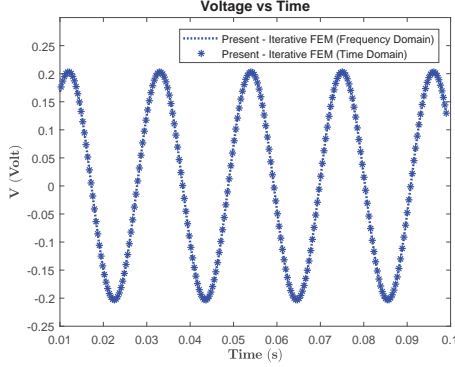| Parameter	Erturk-Inman	Akbar & Curiel-Sosa		Present - Solid		Present - Shell	
$\bar{V}$ (Volt)	0.1979	0.1966	Δ=0.66%	0.1966	Δ=0.66%	0.1952	Δ=1.36%
$\bar{Z}_{rel}$ (mm)	0.0490	-	-	0.0485	Δ=1.02%	0.0484	Δ=1.22%

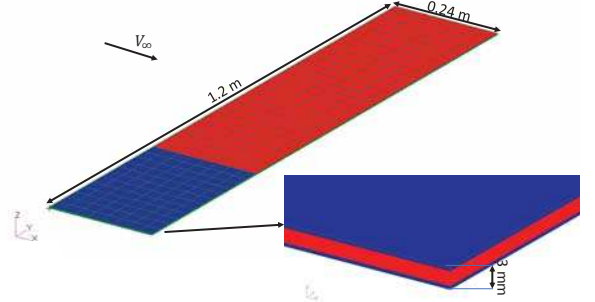Figure 5: The voltage output time history of the unimorph modeled by solid elements

Figure 6: Illustration of a lifting surface exposed to a freestream flow with airspeed V_∞ and 1-cosine gust with maximum gust speed V_{g_0}

$$V_g = \frac{V_{g_0}}{2}\left(1 - cos\frac{2\pi V_\infty t_g}{L_g}\right) \qquad (22)$$

In this section, a plate-like wing with bimorph piezoelectric configuration in [14] is elaborated as the case study. The bimorph plate configuration is depicted in Figure 7. Piezoelectric layers are made of PZT-5A with each covering 30% of the length and 17% of the thickness. The host structure is made of Aluminum and sandwiched between the pieoelectric layers in the region near the root. The PZT-5A layers and Aluminum layers are represented with blue and red regions in Figure 7. The detailed material properties are given in [14].

The PZT-5A layers are combined in a series circuit with each poled in the thickness direction opposite

Figure 7: Configuration of the bimorph

to the other's. A resistance load of 10 kΩ is used to complete the electrical circuit. The whole bimorph plate is assumed as the lifting surface, exposed to a uniform freestream flow at the sea level condition with airspeed, V_∞, parallel to the chordwise direction. The direction from the leading edge to trailing edge is defined as the x-positive direction.

Both solid and shell elements are also applied to model the bimorph plate. The solid finite element model of the bimorph is also shown in Figure 7. The configuration of 40 × 8 elements are used in spanwise and chordwise directions. The same division also applied to the shell model with the different lies on the implementation of laminated composite module to represent the lay-up sequence. To validate the structural model, the natural frequencies and mode shapes of the solid and shell models are compared against the results in [14] as depicted in Table 5.

Table 5: Natural frequency comparison of the bimorph

Mode Shape	Natural Frequency (Hz)				
	FEM [14]	Present - Solid	Δ	Present - Shell	Δ
1B	1.68	1.67	0.59%	1.66	0.60%
2B	10.46	10.43	0.29%	10.36	0.96%
1T	16.66	16.00	3.96%	15.90	4.56%
3B	27.74	27.74	0.00%	27.50	0.22%
2T	48.65	47.02	3.35%	46.67	4.07%

The present models' natural frequencies are well agreed with those obtained via full

9

electromechanically-coupled shell elements in [14]. The variances are considered insignificantly vary from 0.0% to less than 5%. The bending modes are denoted by "1B", "2B" and "3B" while the torsion modes represented by "1T" and "2T". To evaluate aeroelastic loading condition with the freestream flow and gust wind, an unsteady aerodynamic model is coupled with the structural model.

In the present work, the Doublet-Lattice Method (DLM) of Albano and Rodden [50] for subsonic flow is applied to model the aerodynamic loads acting on the lifting surface. The DLM of Albano and Rodden is a well-established approach and commonly implemented in the aircraft industries to evaluate the aeroelastic conditions for certification, i.e., flutter instability and gust loads [49]. In addition, this approach is readily available in commercial software, i.e., MSC Nastran [51].

The DLM discretised the lifting surface into panels in which the aerodynamic forces modelled via doublets concentrated on the quarter chord line of each panel. The doublets' strengths are the function of the unsteady motion of the surface. Thus, applying the modal dynamic analysis to evaluate the structural responses resulted in the aerodynamic forces also as a function of the mode shapes [50]. Therefore, the investigation of the mode shapes are essential to the aeroelastic evaluation.

To verify the coupling of the finite elements and aerodynamic model via DLM, observation on the flutter instability is performed in the present work. The results are compared with those obtained in [15] which evaluate the flutter condition of the same bimorph FEM model in [14].

Figure 8 displays the flutter summary of the bimorph modelled by solid elements. Five mode shapes mentioned in Table 5 are involved in the flutter analysis, the same as used in [15]. However, for clarity, only 3 modes are displayed in 8. Figure 8a depicts the variation of damping ratio to the airspeed, also known as $V - g$ graph in aeroelasticity field. The damping ratio shown here is the total damping ratio due to structural damping and aerodynamic damping. Hence, it changes with the airspeed. The consensus in aeroelasticity field is that negative damping ratio is the stable region, and the positive one is unstable.

Figure 8b shows the variation of the frequency of the aeroelastic system to the airspeed, known as $V - f$ graph. Similar to the damping, the stiffness of the
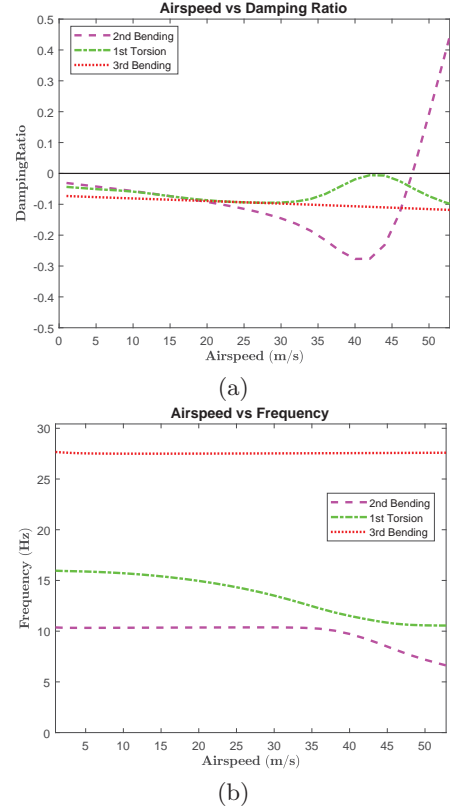

(a)

(b)

Figure 8: (a) Airspeed vs Damping ($V - g$), and (b) Airspeed vs Frequency ($V - f$) graphs of the bimorph

system also changes with the airspeed as the aerodynamic loads also give addition/reduction of the system's stiffness. The critical instability point or the critical flutter speed is reached if the damping ratio of one of the modes become positive or if two or more modes' are coupled.

It can be seen in Figure 8a that the second bending mode crosses the positive region at around 48 m/s. However, in Figure 8b, the the first torsion frequency is decreasing with the airspeed until it coalescences with the second bending frequency at around 40 m/s. Considering these two phenomenons, it can be considered that the critical flutter speed is around 40 m/s. These phenomenons are align with the conditions observed in [15], in which 40 m/s is the critical instability point where the second bending and the first torsion frequencies are found to be coalescence. In addition, identical conditions are also observed via the present shell model.

On the investigation presented in [14], the time-domain Vortex-Lattice Method (VLM) [52] was applied to model the aerodynamic forces. This method is a panel method similar to the DLM with the vortexes' strengths represent the aerodynamic forces.
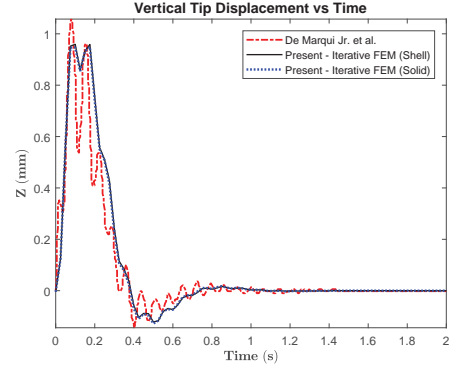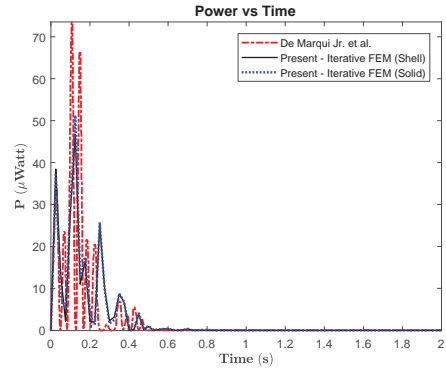
10
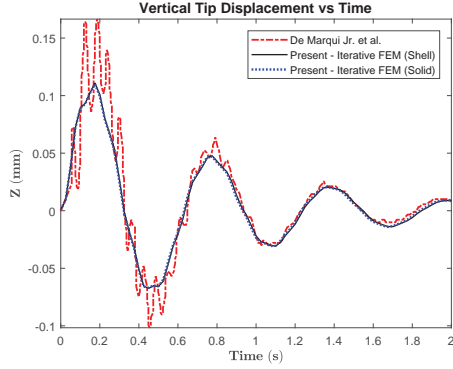
(a)
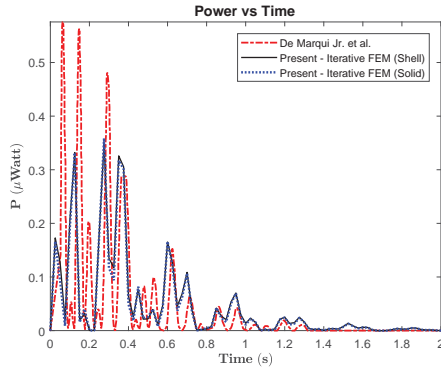
(b)

Figure 9: Time histories of (a) the tip displacement and (b) the power output of the bimorph at 10 m/s airspeed

(a)

(b)

Figure 10: Time histories of (a) the tip displacement and (b) the power output of the bimorph 30 m/s airspeed

However, the VLM is a direct time-domain approach, independent to the mode shapes nor modal analysis. The coupling with the structural model or FEM utilise an iterative procedure to perform a fluid-structure interaction (FSI). The information of the aerodynamic forces is transferred to structure, and the changed structural shape is passed to the aerodynamic model, and so on until the solution converges at a particular time step. To not be confused with the present iterative model, in which the FSI iteration involves only the structural and aerodynamic parts.

A 3° angle of attack, an angle between the freestream flow direction and the chordline cross-sectional direction of the wing/plate, is applied to represent a vertical sharp-edged gust in a very short-time period in [14]. As the detail of the time period nor time steps are not available in [14], a total time period of 0.01 ms is assumed in the present work. The maximum gust velocity, V_{g_0}, is equal with 5.2% V_∞ considering the speed vertical component due to the 3° angle of attack. The gust speed is assumed zero at t_g=0 and suddenly reaches V_{g_0} at 0.01 ms, then becomes zero again after 0.01 ms. Hence, the 1-cosine profile as shown previously in Figure 6 is reduced to

a sharp-edged gust.

Figures 9 and 10 depict time histories of the bimorph′s tip displacements and harvested powers from the piezoelectric layers at 10 m/s and 30 m/s freestream conditions, respectively. The red dashed-dotted lines denote the results of De Marqui Jr. et al. [14]. The final iteration′s results obtained via the present iterative FEM method by shell and solid models are denoted by the black straight lines and the blue dotted lines. The iterative processes for both models are rapidly converge in less than 5 iterations as the harvested voltages do not greatly affect the structural responses. This phenomenon aligns with the results in [14], in which the structural responses from the range of short circuit to open circuit are identical. Thus, showing that the displacement due to mechanical load are much more dominant than the one exerted by the electrical load.

The 10 m/s airspeed condition provides small aerodynamic loads and structural displacement. The maximum tip displacement observed in Figure 9a is significantly in a lower order compared to those obtained at 30 m/s in Figure 10a. However, as larger damping occurs at 30 m/s, the response is rapidly

11

damped after decreasing from the maximum point. In contrast, the one at 10 m/s still oscillating after the first maximum response, showing a moderate damping of the system.

The harvested power responses are aligned with the trends of the tip displacements as shown in Figures 9b and 10b. The harvested power at 10 m/s still oscillating after the first maximum response. However, at 30 m/s, the power response quickly vanishes along with the damped structural response. The VLM simulation and both present models are all in agreement and show similar behaviours. However, it can be seen that the results of the VLM fluctuate with the time due to the FSI iterative process on each time step [52].

In more details, the energy harvested by the three approaches are compared in Table 6. A total time of 2 s is used to calculate the energy harvested. The energies obtained from all approaches are in a good comparison. The present results only vary less than 10% to the results by De Marqui Jr. et al. [14], in which mostly vary between 1% to 4%. Nevertheless, for a preliminary engineering design phase, these variances are considered acceptable.

The displacement contours of the solid bimorph at $t_g = 0.175$ s are depicted in Figures 11a and 11b. At $t_g = 0.175$ s, the loads causes the maximum structural responses for both airspeeds. It can be seen that the second bending mode is dominant in the response with a moderate effect form the torsion mode causes slight twisting to the plate.

Table 6: Electrical energy comparison of the bimorph

Speed (m/s)	FEM [16]	Present - Solid	Δ	Present - Shell	Δ
		Energy (μJ)			
10	0.0865	0.0880	1.73%	0.0927	7.17%
30	5.5295	5.7258	3.55%	5.5838	0.98%

5. UAV wingbox under Gust Load Conditions

The energy harvesting evaluation of a UAV wingbox with a piezoelectric layer is presented in this section. The UAV wingbox configuration in [34] is utilised in the present case. The general configuration of the UAV wingbox, the structural model and the aerodynamic model are displayed in Figure 12.

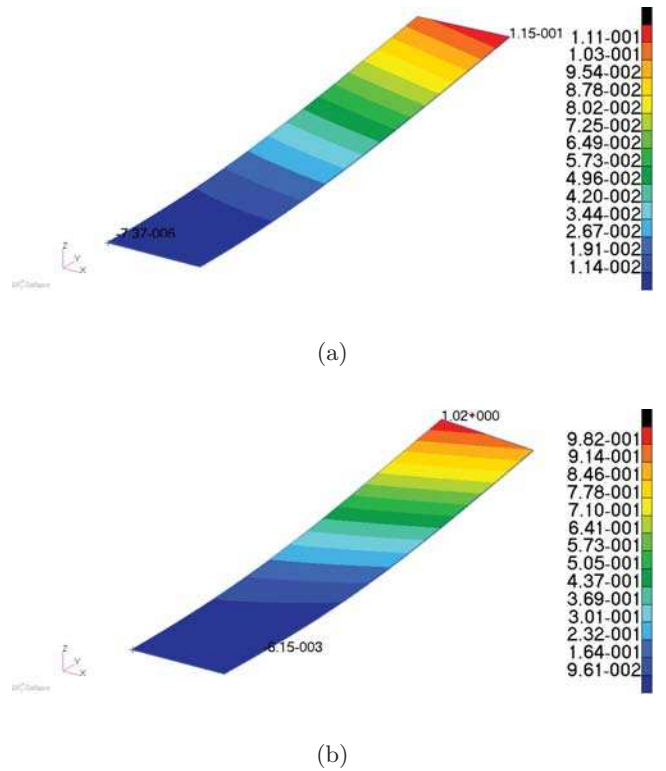In Figure 12, the blue frames depict the structural model via solid elements. The top picture only shows

(a)

(b)

Figure 11: Displacement contours at $t_g = 0.175$ s of the bimorph with airspeeds (a) 10 m/s and (b) 30 m/s (displacemen unit in mm)

the structural model. Meanwhile, the bottom picture shows the finite elements and the aerodynamic panels of DLM, represented by the red frame. In the present case, the aerodynamic panels represent the lifting surface, or the wing surface. However, the structural elements only represent the wingbox. The connection between aerodynamic loads and the structure is contructed via spline interpolation [53]. This is a common practice in aircraft wing's stress or aeroelascticity analyses as the wingbox is the primary load bearing structure in the wing and constructed most of the wing's weight. Hence, if the wingbox can be assured safe, the wing can be assumed safe to carry the primary load, i.e., aerodynamic lift.

The wing has a 5° sweptback angle with 0.9 taper ratio and fixed at the root. The piezoelectric layer is made of PZT-5H, embedded on the top surface of the wingbox. It lies from the root until 10% of the span length. The host structure of the wingbox is aluminum alloy 7075. A more detailed configuration parameters and material properties is referred to the article by Xiang et al. [34]. To validate the structural and aerodynamic models, a flutter investigation of the
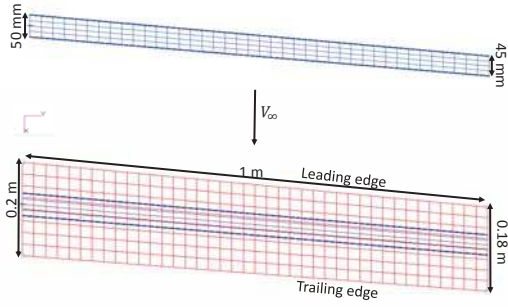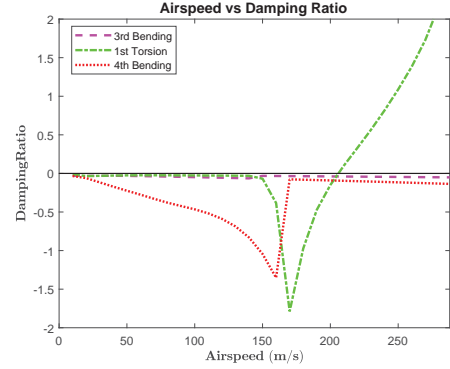
Figure 12: Topside view of the UAV wingbox configuration: Wingbox only - Structural model (top), Wingbox and wing surface - Structural model and aerodynamic panels (bottom)

(a)

(b)

Figure 13: (a) Airspeed vs Damping ($V - g$), and (b) Airspeed vs Frequency ($V - f$) graphs of the UAV wingbox

UAV wing is also performed in the present work. In agreement with flutter observation in [34], sea level condition is assumed, and 6 mode shapes, i.e. four bending modes and two torsion modes, are involved in the analysis. Figure 13 depicted the flutter summary of the UAV wingbox. For clarity purpose, only three main modes coupled to the instability are shown.

Figures 13a and 13a shows the $V - g$ and $V - f$ graphs of the UAV wingbox. It can be seen that the first torsion crosses the positive damping (unstable) region at 220 m/s in Figure 13a. However, the frequency evolution in Figure 13b displays the three modes coalesce at around 140-150 m/s. The frequencies of the third and fourth bending coalesce first at 140 m/s followed by the other intersections. These complete intersections of the three frequencies may lead to a violent instability. This case is known also as a hard flutter condition, while the one for the bimorph in Section 4 is called soft flutter as the frequencies only approach each other at a very short gap [49]. This condition agrees with the critical flutter speed at 150.2 m/s obtained by Xiang et al. [34].

For the gust load condition, the wing is observed at cruise state with $V_\infty = 100$ m/s and flight altitude 4000 m above sea level. The maximum gust velocity, V_{g_0}, is 15% of V_∞ with gust gradient distance, H_g, is 12.5 mean aerodynamic chord (MAC), in this case the total gust time period is 47.5 ms. Extra 1 s observation time is given by Xiang et al. [34] to allow the dynamic response finished. It can be seen, however, the displacement is completely damped after 0.2 s as shown in Figure 14a .

In Figures 14a and 14b the responses of both the present result and those obtained in [34] are in a good agreement at the beginning until it reach the maxi-

mum responses. However, some discrepancies can be seen after the first maximum responses. The displacement obtained by Xiang et al. [34] is damped quickly without any oscillation after it reaches the first amplitude. In contrast, the present result shows at least a few damped oscillation after the first amplitude.
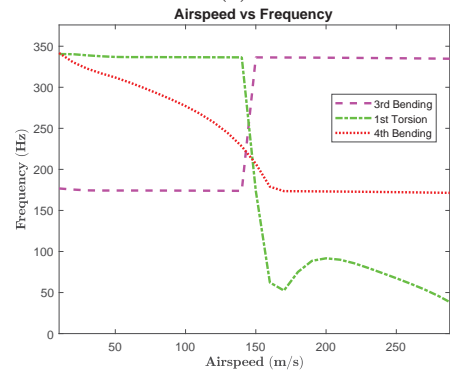
This discrepancy may occur due to different structural and aerodynamic models used by both method. Xiang et al. used beam model with discrete masses calculated from the step function. Moreover, the strip theory is used to model the unsteady aerodynamic load [34]. It has been discussed in the literature [51], in a classic aeroelastic benchmark of the BAH wing [54] shows the use of the strip theory may give an overdamped response compared to the one with DLM.

In contrast, Figure 14b shows the result of Xiang et al. still produces voltage output even though the displacement is completely damped. Meanwhile, the present voltage output is in agreement with the displacement response. The voltage output still oscillating after it reaches the first amplitude. This behaviour is much more consistent with those shown in Section 4 and later on observed in Section6, in which

13
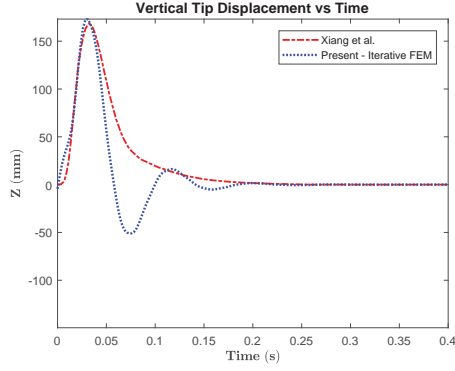
(a)
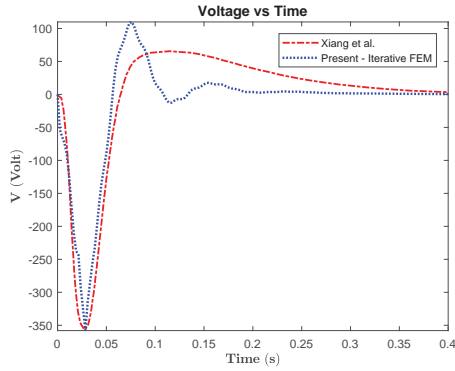
(b)

Figure 14: Time histories of (a) the tip displacement and (b) the voltage output of the UAV wingbox under 1-cosine gust

the electrical responses follow the similar trend with the displacement responses.
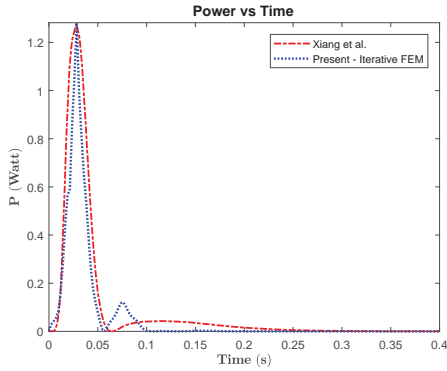

Figure 15: The power output time history

Figure 15 shows the power response of the present model still has fluctuations after the first maximum power although the second largest fluctuation only sustained around 0.05 s. Meanwhile, after the first amplitude, the result from Xiang et al. sustained a lower maximum power which sustained much longer, around 0.15 s. This behaviour resulted in a discrepancy of the total energy output. The present result only achieve 25.3 mJ compared to the one obtained
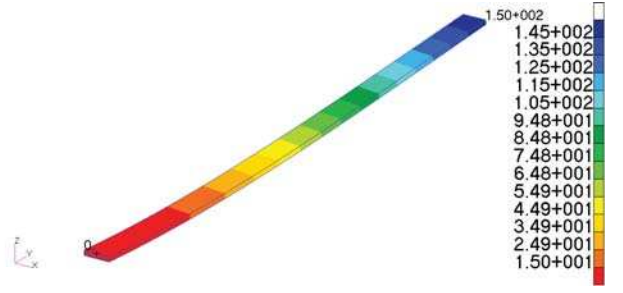

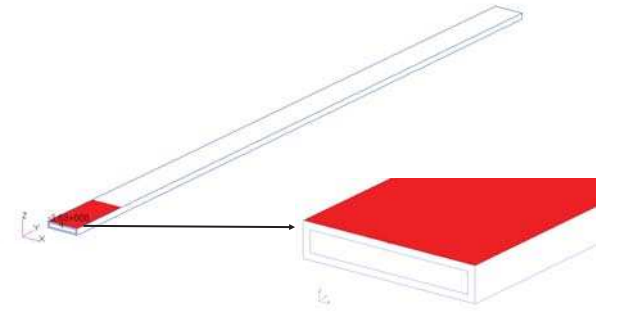Figure 16: Displacement contour of the UAV wingbox at $t_g = 0.0285$ s(displacement unit in mm)

Figure 17: Voltage contour of the piezoelectric layer of the UAV wingbox at $t_g = 0.0285$ s (voltage unit in μV)

by Xiang et al., 35.1 mJ.

A detailed displacement contour of the UAV wingbox at $t_g = 28.5$ ms is depicted in Figure 16. At $t_g = 28.5$ ms, the maximum displacement response is exerted by the combined mechanical and electrical loads. The displacement is mostly dominated by the first bending mode where the maximum is observed at the tip. Figure 17 shows the voltage contour on the wingbox. It is obviously seen that the voltage only occurs at the thin top layer near the root in which the piezoelectric is located. An amount of 363 Volt is observed at $t_g = 28$ ms. Meanwhile, the other parts of the wingbox do not produce the voltage as there is no electromechanical coupling.

Figure 18 displays the voltage responses at different iteration steps. It can be seen the responses for all the steps are almost coincide. In the enlarged view, the result from the second iteration is shown slightly overestimates the other results. The third and the fourth iteration results, however, are still almost coincide even in the enlarged view. In more details, the iterative process is shown in Table 7. The harvested energy even only after the third iteration provided
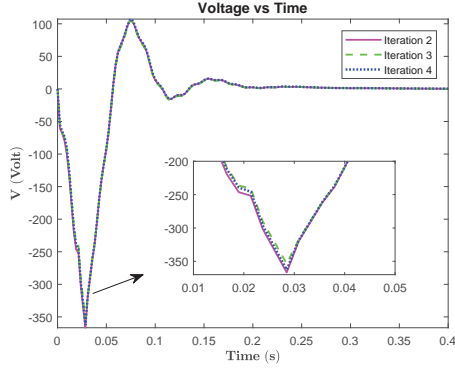
Figure 18: The voltage output time histories at different iteration steps

less than 5% iteration variance. After ten iteration, the iteration variance even lower, with value less than 1%. This shows that the displacement due to electrical load also insignificant to the one exerted by the mechanical load. This behaviour is similar with the results observed on Section 4. In this case, it might can be considered that the normal flight operation with active piezoelectric energy harvesting may not provide significant change to the structural deformation while still may produce voltage response. Further this behaviour is also observed in Section 6.

Table 7: Electrical energy output of the UAV wingbox on each iteration step

Iteration	Energy (J)	Variance
1	0.0250	
2	0.0263	$\Delta_{1-2} = 5.60\%$
3	0.0250	$\Delta_{2-3} = 4.94\%$
4	0.0256	$\Delta_{3-4} = 2.40\%$
9	0.0251	
10	0.0253	$\Delta_{9-10} = 0.79\%$

6. Jet aircraft wingbox under Gust Load Condition

The energy harvesting investigation for a notional civil jet aircraft wingbox is presented in this section. The typical 1-cosine gust is applied as the excitation load acting on the wingbox. The aircraft wingbox model used in the present work is based on the configuration in [38]. However, some modifications are employed in the present work, in order to have a more realistic configuration similar to those in a typical long-range flight aircraft, i.e., Boeing 737-800. A 30° sweptback modification based on a typical jet aircraft

wing in [55] is applied. The wingbox layout including the structural and aerodynamic models from topside view are shown in Figure 19.

The blue frames on the left and right sides of Figure 19 represent the structural parts of the wingbox modelled via shell elements. The thickness for the ribs and the spars is 7.04 mm, while for the skins is 6.09 inches. An addition of an inner wingbox part as the connection to the fuselage is employed here to construct the swept configuration. In [38], the root chord was the one with 2.29 m chord length, and this is the location of the cantilevered boundary condition. However, in the current case, the fixed root is the one with 2.65 m chord length.

Originally, all of the wingbox materials are Aluminium Alloy, Al-2219, with density 2840 kg/m^3 and Young's modulus 73.1 GPa. For energy harvesting purpose, the upper skin material is replaced by PZT-5A. The upper skin is modeled as unidirectional laminated via shell elements with piezoelectric 1-direction lies on the midchord span. The wingbox configuration with PZT-5A as the upper skin has been shown to have a maximum energy harvesting potential around 40 kW [39]. However, the investigation in [39] assumed a harmonic load constructed from the steady aerodynamic cruise lift and excitation frequency near the first bending frequency. This loading scenario was very much simplified compared to a real flight scenario. Therefore, in the present case, with the existence of gust load and the implementation of unsteady aerodynamic model, the evaluation on how much this harvesting potential can be achieved is discussed on a later part of this section.

The first bending natural frequency of the present wingbox is 1.72 Hz, slightly increases from the one in [39] by 6.8% due to additional stiffness from the inner wingbox part at the root. Along with the first bending, other mode shapes of the wingbox are shown in Figure 20. The natural frequencies of the second bending and the first torsion shown in Figure 20 are 7.36 Hz and 23.47 Hz, respectively. The mix bending and torsion mode shown is the 7th mode of the wingbox at 31.50 Hz, following this mode, the higher modes are the combination of two or more basic modes. In the present case, flutter analysis is performed to observe the frequency and damping evolution as the functions of airspeed.

The red frame in Figure 19 depicts the wing surface divided into a number of aerodynamic panels. Similar to the case of UAV wingbox in Section 5, the aircraft
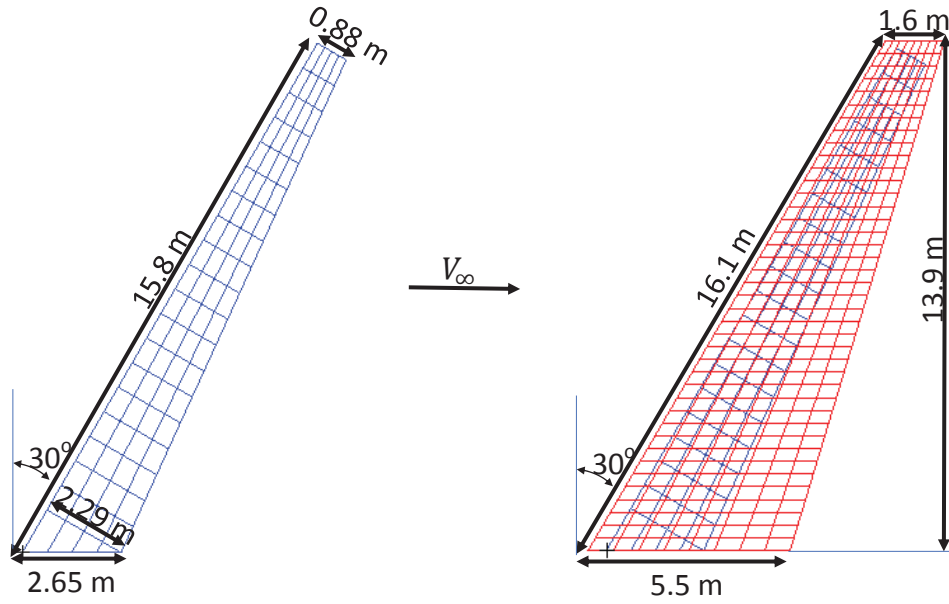
15

Figure 19: Topside view of the aircraft wingbox configuration: Wingbox only - Structural model (left), Wingbox and wing surface - Structural model and aerodynamic panels (right)
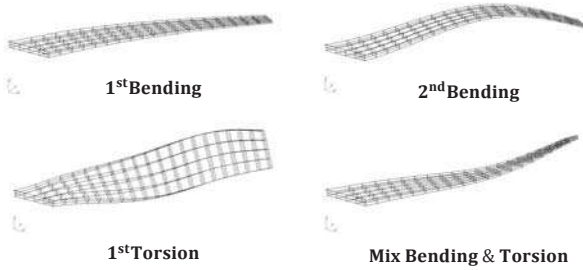

Figure 20: Mode shapes the aircraft wingbox

wing represented by the aerodynamic panels covering a much larger surface than the structural elements. Ten modes are involved in the analysis to accommodate any influence from the high frequency modes. The flutter analysis is performed at the cruise altitude, around 10000 m above sea level, with the speed of sound (Mach 1) around 300 m/s. Therefore, the flutter analysis is limited to this speed as the DLM here only applicable for subsonic regime. The flutter summaries in the form of $V - g$ and $V - f$ graphs are shown in Figure 21.

It can be observed in both Figures 21a and 21b that neither the dampings nor the frequencies show any sign of instability, flutter does not occur at the subsonic regime. Although several behaviours can be observed going towards instability, i.e., the damping curve of the first bending starts going up just before 300 m/s, the first bending frequency approaching the second bending, and the first torsion frequency starts declining.

Nevertheless, assuming 0.8 Mach (240 m/s) cruise speed, it is understandable that the critical flutter speed will be beyond 300 m/s. According to FAR 25, The dive speed which is the maximum aircraft speed limit on the flight envelope required to be 1.15 of the cruise speed. While, the critical flutter speed is 1.15 of the dive speed. Hence, the dive speed will be 276 m/s and the minimum allowable critical flutter speed is 317 m/s (Mach 1.06).

In the gust loading simulation, the cruise condition and the discrete 1-cosine gust are applied. Based on FAR 25, the range of the gust gradient for discrete gust load evaluation are from 30 ft (9 m) to 350 ft (107 m). In the present case, three different gust gradient distances, H_g, 30 ft, 350 ft and a typical value of 12.5 MAC (43 m) are evaluated.

Concerning a daily average of maximum gust condition in the United Kingdom area [56], 15 m/s is chosen as the gust speed amplitude, V_{g_0}. To complete the
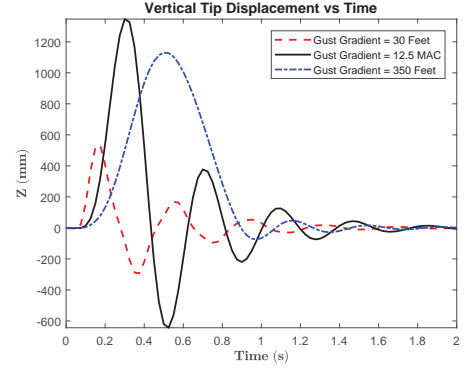
16
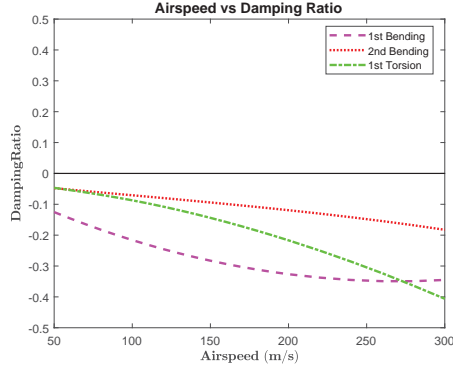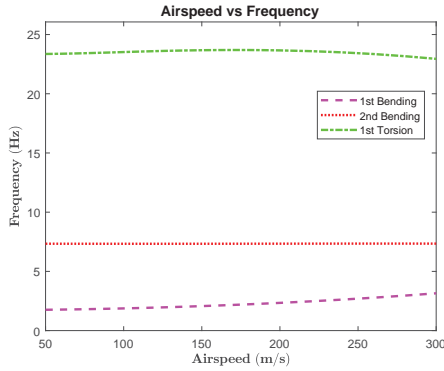
Figure 21: (a) Airspeed vs Damping $(V - g)$, and (b) Airspeed vs Frequency $(V - f)$ graphs of the aircraft wingbox

Figure 22: The time histories of (a) vertical tip displacment and (b) voltage output of the aircraft wingbox for different gust gradient distances with gust velocity 15 m/s
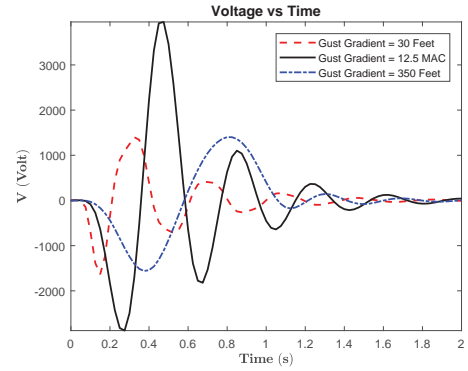
energy harvesting system, 1250 Ω of resistance load is connected. This value of resistance load gives an optimum power for all three gust distances. Figure 22 displays the displacement and voltage responses for the three H_g conditions.

It can be seen in Figure 22a that the shortest distance gives the smallest amplitude while 12.5 MAC distance provides the largest amplitude. At $H_g = 9$ m, the disturbance only has a sort time period, 75 ms, to affect the structure. In contrast, at $H_g = 107$ m, the gust load penetrates the structure almost 1 s, allowing a slope response gradient or a low velocity response. In this case, after the disturbance, the response almost smoothly damped without oscillating. However, at $H_g = 12.5$ MAC, the disturbance is sustained long enough to gives the maximum amplitude. While it still keeps a steep displacement gradient or a high velocity response, hence, it allows some oscillations after the gust ended.

In Figure 22b, it is interesting to see that the shortest and the longest distances resulted in a similar level of maximum voltage. These behaviours are due to the shortest distance gives the smallest displacement amplitude while a slope response exerted by the longest

distance resulted in the smallest velocity amplitude. Moreover, at $H_g = 12.5$ MAC, the maximum voltage amplitude is achieved as it gives the maximum displacement and velocity.

The power output as depicted in Figure 23 also reflected similar behaviours as the shortest and the longest distances give a similar level of amplitude, while at $H_g = 12.5$ MAC, the maximum power amplitude is obtained. As expected, the largest energy is harvested at $H_g = 12.5$ MAC as shown in Table 8.

Table 8: Electrical energy output of the aircraft wingbox for different gust gradient distance with gust velocity 15 m/s

H_g	Energy (kJ)
30 ft (9 m)	0.3767
12.5 MAC (43 m)	2.4921
350 ft (107 m)	0.7639

The voltage output at different iteration steps are shown in Figure 24. It can be seen that the responses from three iteration steps are hardly distinguished. In the enlarged view, the first iteration, denoted by pink dashed line, is just slightly overestimates the
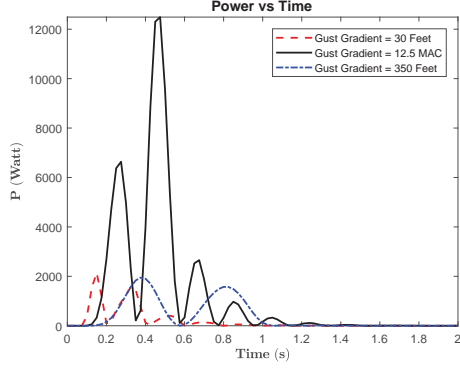
Figure 23: The power output time history of the aircraft wingbox for different gust gradient distance with gust velocity 15 m/s

second and third iterations. After the first iteration, the responses declined at the second iteration, and then slightly going up again at the third iteration.
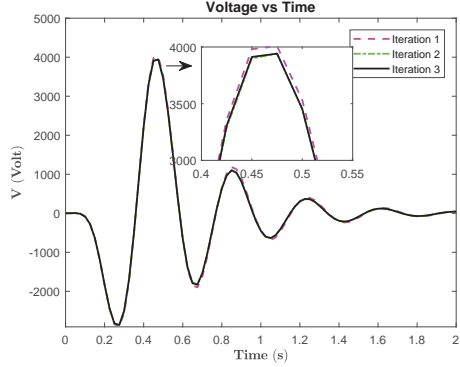

Figure 24: The voltage output time history of the aircraft wingbox with gust gradient distance 12.5 MAC at different iteration step

In more details, Table 9 displays the iteration process in terms of the energy output. The first to the second iteration variance is only around 5%, followed by less than 1% variance after third iteration. This trend is in agreement with the one shown in Section 5. In this case, the mechanical load dominated the displacement response, and the reverse piezoelectric effect may not be significantly affects the structural response.

The voltage contour of the wingbox is shown in Figure 25. It shows the response for $H_g = 12.5$ MAC and $V_{g_0} = 15$ m/s. At $t_g = 0.3$ s, the gust loading exerted the maximum displacement response of the wingbox. It can be seen that the maximum voltage of 3.95 kV only occur at the upper skin made of PZT-5A and the other parts do not produce any voltage.

For comparison, the maximum power achieved for $H_g = 12.5$ MAC and $V_{g_0} = 15$ m/s, is around 12

Table 9: Electrical energy output of the aircraft wingbox on each iteration step

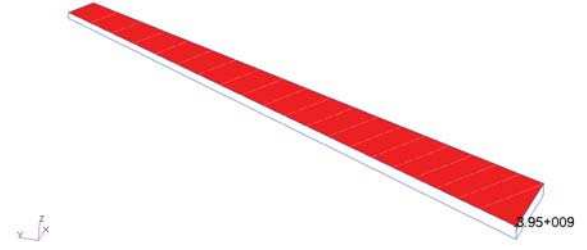| Iteration	Energy (kJ)	Variance
1	2.6093	
2	2.4752	$\Delta_{1-2} = 5.14\%$
3	2.4991	$\Delta_{2-3} = 0.97\%$
4	2.4884	$\Delta_{3-4} = 0.43\%$
5	2.4921	$\Delta_{4-5} = 0.15\%$

Figure 25: Voltage contour of the aircraft wingbox for 12.5 MAC gust gradient distance with gust velocity 15 m/s at $t_g = 0.3$ s (voltage unit in μV)

kw, a similar order of power with the one obtained via hybrid analytical/FEM scheme in [39] for a harmonic cruise load with excitation at 0.8 first bending frequency. However, it is still smaller than the one achieved with 0.9 first bending frequency. Hence, to observe a larger potential of the wing, another scenario with the same gust distance but larger gust speed is evaluated. An average of moderate gust speed in the United Kingdom area, 30 m/s [56], is selected as the V_{g_0}. The displacement and voltage responses for the two different speeds are depicted in Figure 26.

It is easily seen from Figure 26 that with the same gust gradient distance, both gust speeds possess a similar pattern of time histories. However, with a larger gust speed amplitude, 30 m/s, the amplitudes of the displacement and voltage are also higher. As displayed in Figure 27, In agreement with these trends, the power output for $V_{g_0} = 30$ m/s is also higher than the one obtained for 15 m/s.

The maximum power for $V_{g_0} = 30$ m/s reaches around 51 kW. This is larger than the one obtained in [39], around 40 kW for excitation at 0.9 first bending frequency. Hence, despite the fact that different approaches are used, the present results strengthen the findings obtained in [39]. The potential of piezo-

18

Vertical Tip Displacement vs Time

(a)

Voltage vs Time
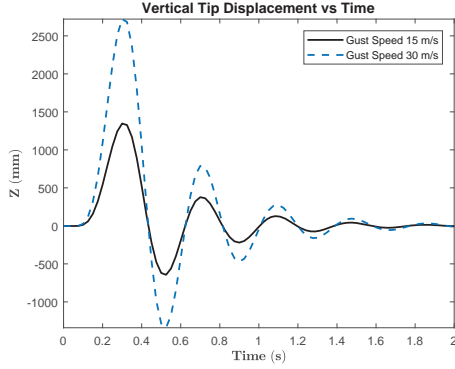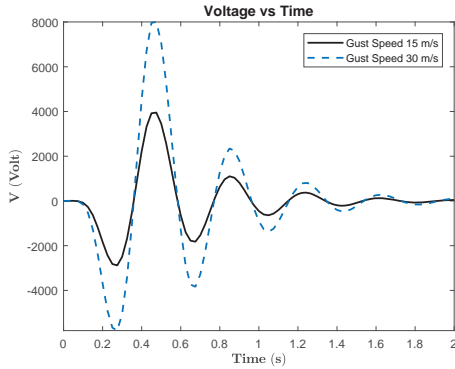
(b)

Figure 26: The time histories of (a) vertical tip displacement and (b) voltage output of the aircraft wingbox for different gust velocities with gust gradient distance 12.5 MAC

electric energy harvesting from the typical jet aircraft wingbox may reach an order of tens kW of power.

In the present work, concerning the structural strength, for the first time, the stress and failure analyses of the structure due to the flight condition and the harvested electrical power are performed. The present iterative FEM provides an ease of commercial software utilisation, hence, several analysis modules can be explored to support the observation of the energy harvesting structure. In the present case, the gust and failure analysis modules are implemented together, hence, the failure index of the wingbox with active energy harvesting during the gust loading can be observed.

Figures 28a and 28b show the vwertical displacement contours of the wingbox for $V_{g_0} = 15$ m/s and $V_{g_0} = 30$ m/s. It can be seen that the displacements for both speed are mostly influenced by the first bending mode, with a slight twist as the effect from the torsion mode. The maximum displacements at the tip are 1.35 m and 2.73 m for $V_{g_0} = 15$ m/s and $V_{g_0} = 30$ m/s, respectively. The maximum principal stress contours in relation to these displacements can
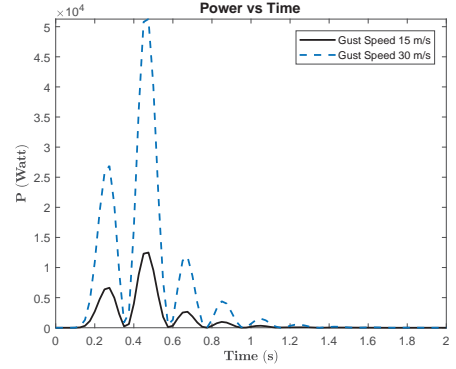

Figure 27: The power output time history of the aircraft wingbox for different gust velocity with gust gradient distance 12.5 MAC

be seen in Figures 29a and 29b.

From the stress contours, compression at the upper skin and tension at the lower skin can be seen as the wingbox vertically bends upward. It can be seen that the stress concentrations occur at the lower skin′ trailing edge near the root. The maximum stress is doubled from $V_{g_0} = 15$ m/s to 30 m/s as depicted from Figures 29a and 29b. Concerning the yield strength and ultimate strengths of Al-2219 are 352 MPa and 455 MPa [57], the condition for both gust speeds are still in the regime of linear elastic. In addition, the stresses on the upper skin also still in a much lower level of the PZT-5A yield strength, 140 MPa [58].

The failure analysis of the wingbox is performed using the Tsai-Wu theory. The convention of the failure index 0-1 is used. The yield and tensile strengths of the materials are concerned. To be noted that the PZT-5A is a brittle material, hence, the yield and tensile strengths are the same [58]. The index 0 shows there is no damage on the structure, while index 1 denotes a full failure.

Figures 29c and 29c depict that the maximum failure index for $V_{g_0} = 30$ m/s are four times the index for $V_{g_0} = 15$ m/s, from 0.143 to 0.575. Despite this fact, the maximum failure indices are still less than 1. Hence, even with 30 m/s gust amplitude, the wingbox structure is considered safe. In addition, the failure indices at the upper skin also relatively small, less than 0.1. Therefore, it can be assumed that the piezoelectric layer are in a very safe condition.

7. Conclusion

A novel iterative finite element method (FEM) for energy harvesting purpose has been developed. The
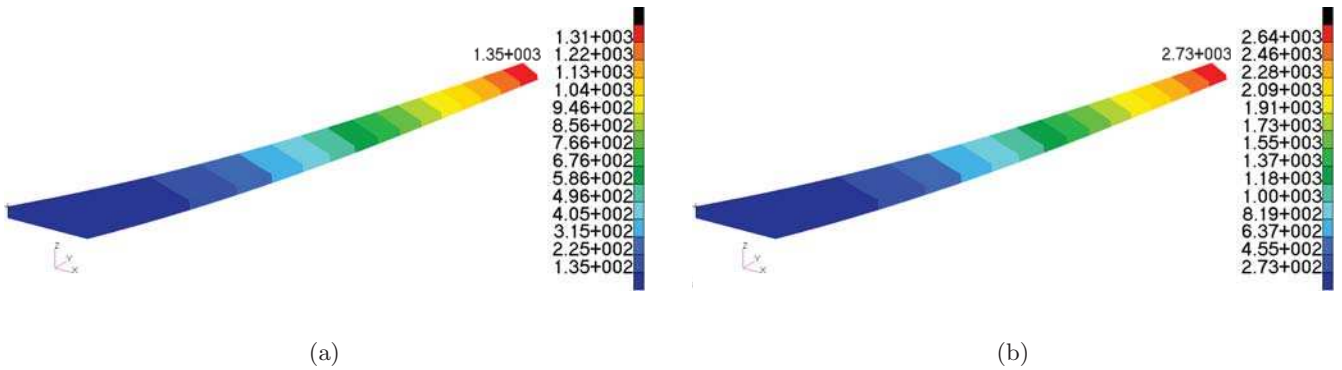
19

Figure 28: Displacement contours of the aircraft wingbox for 12.5 MAC gust gradient distance with (a) 15 m/s and (b) 30 m/s gust velocities at $t_g = 0.3$ s (displacement unit: mm)

computational code based on this new iterative FEM has been built for the dynamic problems in the frequency and time domains. Validation with the classical benchmark of piezoelectric energy harvester plate under base excitation shows an excellent agreement both in frequency and time domains.

Three different lifting structures, i.e., a plate-like wing, a UAV wingbox, and a transport aircraft wingbox, with active energy harvesting layer(s) subjected to 1-cosine gusts are investigated via the time-domain iterative FEM. Based on the three cases, the iterative processes are considerably fast, and convergences are achieved in less than ten iterations. The results are all showing similar behaviours with the references′.

From the observation on the iterative processes, an exciting finding is taken, the responses of all the lifting structures are dominated by the mechanically-exerted displacements. The influences of the reverse piezoelectric effect are minimum. Hence, for normal flight operation, it may occur that the displacement is not significantly affected by the harvested voltage. Thus, the selection or tuning of the resistance load is essential to achieve the optimum power.

Implementation of the iterative FEM to a transport aircraft wingbox with 14.5 m half span shows a promising power output up to 51 kW. This result supports the one obtained via the hybrid analytical/FEM in the literature [39]. In the literature, this level of maximum power output has been proven may support the Auxiliary Power Unit (APU) operation of the aircraft.

The utilisation of the commercial software in the iterative FEM has given the flexibility to implement several types of structural analysis, i.e., gust and failure modules. In the present work, the stress and failure analyses of the aircraft wingbox while subjected to the gust load and harvesting the energy have been conducted. The failure analysis depicts that the wingbox is safe even when it is subjected to a 30 m/s gust amplitude while harvesting 51 kW power. These results have shown that the multidisciplinary problems, i.e., aeroelastic vibration, energy harvesting and structural strength, as mentioned in the literature [38, 39] can be overcome with this iterative FEM.

However, to be noted that in the present work, a continuous electrode is assumed, thus, uniform voltage distribution is expected. In a real case, manufacturing capability and materials availability may need to be considered. Hence, a discrete segmentation of the piezoelectric layer may be required. Furthermore, considering the failure analysis, fracture and delamination in the piezoelectric composite laminates [59] may need to be addressed in the future, as well as the fracture during flight operation [60]. In addition, an evaluation on continuous gust or turbulence disturbance may also be considered for the future works.

Acknowledgements

References

[1] Thomas JP, Qidwai MA, Kellogg JC. Energy scavenging for small-scale unmanned systems. J Power Sources
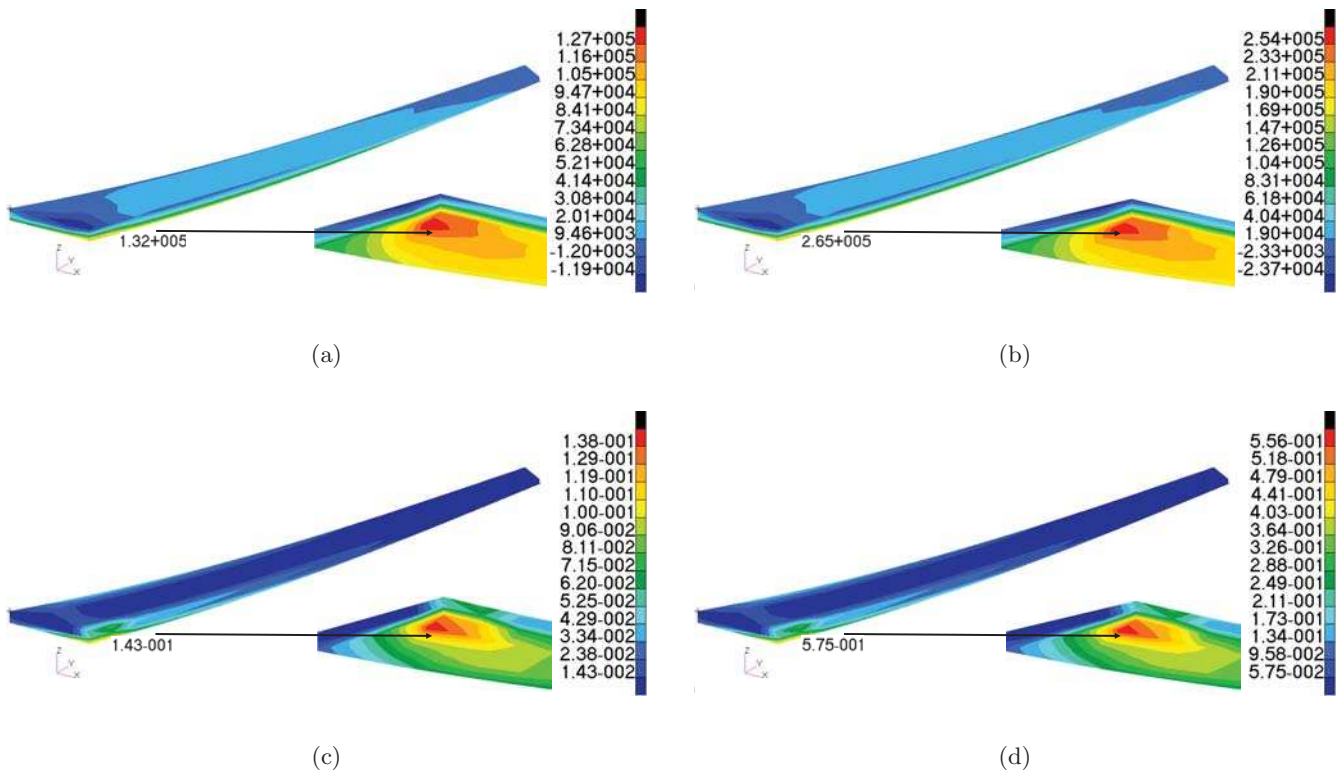
20

Figure 29: The stress contours with (a) $V_{g_0} = 15$ m/s, (b) $V_{g_0} = 30$ m/s; and the failure indices with (c) $V_{g_0} = 15$ m/s, (d) $V_{g_0} = 30$ m/s of the aircraft wingbox for $H_g = 12.5$ MAC at $t_g = 0.3$ s

2006;159(2):1494 –509.

[2] Selvan KV, Mohamed Ali MS. Micro-scale energy harvesting devices: Review of methodological performances in the last decade. Renew Sustain Energy Rev 2016;54:1035 –47.

[3] Hafizh H, Hamsan R, Zamri AAA, Keprawi MFM, Shirato H. Solar updraft power generator with radial and curved vanes. AIP Conf Proc 2018;1930(1):020018.

[4] Ferreira ADB, Nvoa PR, Marques AT. Multifunctional material systems: A state-of-the-art review. Compos Struct 2016;151:3 – 35.

[5] Sairajan K, Aglietti G, Mani K. A review of multifunctional structure technology for aerospace applications. Acta Astronaut 2016;120:30 – 42.

[6] Anton SR, Inman DJ. Vibration energy harvesting for unmanned aerial vehicles. Proc SPIE Act Passiv Smart Struct Integr Syst 2008;6928:692824.

[7] Li D, Wu Y, Ronch AD, Xiang J. Energy harvesting by means of flow-induced vibrations on aerospace vehicles. Prog Aerosp Sci 2016;86:28 – 62.

[8] Abdelkefi A. Aeroelastic energy harvesting: A review. Int J Eng Sci 2016;100:112–35.

[9] Erturk A, Vieira WGR, De Marqui Jr. C, Inman DJ. On the energy harvesting potential of piezoaeroelastic systems. Appl Phys Lett 2010;96(18):184103.

[10] De Marqui Jr. C, Erturk A. Electroaeroelastic analysis of airfoil-based wind energy harvesting using piezoelectric transduction and electromagnetic induction. J Intell Mater Syst Struct 2013;24(7):846–54.

[11] Dias JAC, De Marqui C, Erturk A. Hybrid piezoelectric-inductive flow energy harvesting and dimensionless electroaeroelastic analysis for scaling. Appl Phys Lett 2013;102(4):044101.

[12] Dias JAC, De Marqui Jr. C, Erturk A. Three-degree-of-freedom hybrid piezoelectric-inductive aeroelastic energy harvester exploiting a control surface. AIAA J 2015;53(2):394–404.

[13] De Marqui Jr. C, Maria MJ. Effect of piezoelectric energy harvesting on the response of a generator wing to a turbulence gust. In: 27th Congress of The International Council of The Aeronautical Sciences. 2010,.

[14] De Marqui Jr. C, Erturk A, Inman DJ. Piezoaeroelastic modeling and analysis of a generator wing with continuous and segmented electrodes. J Intell Mater Syst Struct 2010;21(10):983–93.

[15] De Marqui Jr. C, Vieira WGR, Erturk A, Inman DJ. Modeling and analysis of piezoelectric energy harvesting from aeroelastic vibrations using the Doublet-Lattice Method. J Vib Acoust 2011;133(1):011003.

[16] De Marqui Jr. C, Erturk A, Inman DJ. An electromechanical finite element model for piezoelectric energy harvester plates. J Sound Vib 2009;327(1):9 – 25.

[17] Amini Y, Emdad H, Farid M. Finite element modeling of functionally graded piezoelectric harvesters. Compos Struct 2015;129:165–76.

[18] Amini Y, Fatehi P, Heshmati M, Parandvar H. Time domain and frequency domain analysis of functionally graded piezoelectric harvesters subjected to random vibration: Finite element modeling. Compos Struct

2016;136:384–93.

[19] Shindo Y, Narita F. Dynamic bending/torsion and output power of s-shaped piezoelectric energy harvesters. Int J Mech Mater Des 2014;10(3):305–11.

[20] Lee H, Sharpes N, Abdelmoula H, Abdelkefi A, Priya S. Higher power generation from torsion-dominant mode in a zigzag shaped two-dimensional energy harvester. Applied Energy 2018;216:494 – 503.

[21] Muthalif AG, Nordin ND. Optimal piezoelectric beam shape for single and broadband vibration energy harvesting: Modeling, simulation and experimental results. Mechanical Systems and Signal Processing 2015;54-55:417 – 26.

[22] Chen Y, Mu X, Wang T, Ren W, Yang Y, Wang ZL, et al. Flutter phenomenon in flow driven energy harvestera unified theoretical model for stiff and flexible materials. Scientific Reports 2016;6.

[23] Aquino AI, Calautit JK, Hughes BR. Evaluation of the integration of the wind-induced flutter energy harvester (wifeh) into the built environment: Experimental and numerical analysis. Applied Energy 2017;207:61 – 77.

[24] Meiling Zhu E, Worthington J, Njuguna J. Analyses of power output of piezoelectric energy-harvesting devices directly connected to a load resistor using a coupled piezoelectric-circuit finite element method. IEEE T Ultrason Ferr 2009;56(7):1309–18.

[25] Yang Y, Tang L. Equivalent circuit modeling of piezoelectric energy harvesters. J Intell Mater Syst Struct 2009;20(18):2223–35.

[26] Wu PH, Shu YC. Finite element modeling of electrically rectified piezoelectric energy harvesters. Smart Mater Struct 2015;24(9):094008.

[27] Gedeon D, Rupitsch SJ. Finite element based system simulation for piezoelectric vibration energy harvesting devices. J Intell Mater Syst Struct 2018;29(7):1333–47.

[28] Gafforelli G, Ardito R, Corigliano A. Improved one-dimensional model of piezoelectric laminates for energy harvesters including three dimensional effects. Compos Struct 2015;127:369 –81.

[29] Fattahi I, Mirdamadi HR. Novel composite finite element model for piezoelectric energy harvesters based on 3D beam kinematics. Compos Struct 2017;179:161 –71.

[30] Amini Y, Emdad H, Farid M. An accurate model for numerical prediction of piezoelectric energy harvesting from fluid structure interaction problems. Smart Mater Struct 2014;23(9):095034.

[31] Rostami AB, Armandei M. Renewable energy harvesting by vortex-induced motions: Review and benchmarking of technologies. Renew Sust Energ Rev 2017;70:193 – 214.

[32] Wei C, Jing X. A comprehensive review on vibration energy harvesting: Modelling and realization. Renew Sust Energ Rev 2017;74:1 – 18.

[33] Bashir M, Rajendran P, Khan S. Energy harvesting from aerodynamic instabilities: Current prospect and future trends. IOP Conf Ser-Mat Sci 2018;290:012054.

[34] Xiang J, Wu Y, Li D. Energy harvesting from the discrete gust response of a piezoaeroelastic wing: Modeling and performance evaluation. J Sound Vib 2015;343:176–93.

[35] Bruni C, Gibert J, Frulla G, Cestino E, Marzocca P. Energy harvesting from aeroelastic vibrations induced by discrete gust loads. J Intel Mat Syst Str 2017;28(1):47–62.

[36] Tsushima N, Su W. Modeling of highly flexible mul-

[37] Tsushima N, Su W. Concurrent active piezoelectric control and energy harvesting of highly flexible multifunctional wings. J Aircraft 2017;54(2):724–36.

[38] Akbar M, Curiel-Sosa JL. Piezoelectric energy harvester composite under dynamic bending with implementation to aircraft wingbox structure. Compos Struct 2016;153:193 – 203.

[39] Akbar M, Curiel-Sosa J. Implementation of multiphase piezoelectric composites energy harvester on aircraft wingbox structure with fuel saving evaluation. Compos Struct 2018;.

[40] Akbar M, Curiel-Sosa JL. Evaluation of piezoelectric energy harvester under dynamic bending by means of hybrid mathematical/isogeometric analysis. Int J Mech Mater Des 2017;.

[41] Erturk A, Inman DJ. A distributed parameter electromechanical model for cantilevered piezoelectric energy harvesters. J Vib Acoust 2008;130(4):041002.

[42] Standards Committee of the IEEE Ultrasonics, Ferroelectrics, and Frequency Control Society . IEEE Standard on Piezoelectricity. ANSI/IEEE Std 176-1987 1988;.

[43] Freed BD, Babuska V. Finite element modeling of composite piezoelectric structures with MSC/NASTRAN. Proc SPIE 1997;3041:676–88.

[44] Cote F, Masson P, Mrad N, Cotoni V. Dynamic and static modelling of piezoelectric composite structures using a thermal analogy with MSC/NASTRAN. Compos Struct 2004;65(3):471 –84.

[45] Rao S. The Finite Element Method in Engineering. Elsevier Butterworth Heinemann; 2005. ISBN 9780750678285.

[46] Staworko M, Uhl T. Modeling and simulation of piezoelectric elements-comparison of available methods and tools. Mech 2008;27(4):161–71.

[47] MSC Nastran 2014 Dynamic Analysis User's Guide. MSC Software Corporation; 2014.

[48] Erturk A, Inman DJ. Piezoelectric Energy Harvesting. John Wiley & Sons, Ltd.; 2011.

[49] Wright JR, Cooper JE. Introduction to Aircraft Aeroelasticity and Loads. John Wiley & Sons, Ltd.; 2007.

[50] Albano E, Rodden WP. A doublet-lattice method for calculating lift distributions on oscillating surfaces in subsonic flows. AIAA J 1969;7(2):279–85.

[51] MSC Nastran Version 68 Aeroelastic Analysis User's Guide. MSC Software Corporation; 2002.

[52] Katz J, Plotkin A. Low Speed Aerodynamics. Cambridge University Press; 2001.

[53] Harder R, Desmarais R. Interpolation using surface splines. J Aircraft 1972;9(2):189–91.

[54] Bisplinghoff RL, Ashley H, L.Halfman R. Aeroelasticity. Dover Publications, Inc.; 1983.

[55] Ainsworth J, Collier C, Yarrington P, Lucking R, Locke J. Airframe wingbox preliminary design and weight prediction. In: 69th Annual Conference on Mass Properties, Virginia Beach, Virginia. 2010, p. 41.

[56] Hewston R, Dorling SR. An analysis of observed daily maximum wind gusts in the uk. J Wind Eng Ind Aerodyn 2011;99(8):845 –56.

[57] http://asm.matweb.com/; Accessed: June 2018.

[58] Anton SR, Erturk A, Inman DJ. Bending strength of piezoelectric ceramics and single crystals for multifunc-

tional load-bearing applications. IEEE T Ultrason Ferr 2012;59(6):1085 –92.

[59] Curiel-Sosa J, Tafazzolimoghaddam B, Zhang C. Modelling fracture and delamination in composite laminates: Energy release rate and interface stress. Compos Struct 2018;189:641 –7.

[60] Abdullah NA, Curiel-Sosa JL, Akbar M. Aeroelastic assessment of cracked composite plate by means of fully coupled finite element and doublet lattice method. Compos Struct 2018;.